Mapping the per-residue surface electrostatic potential of CAPRIN1 along its phase-separation trajectory

Yuki Toyama[a,b,c,1,2] , Atul Kaushik Rangadurai[a,b,c,d,1], Julie D. Forman-Kay[d,b] , and Lewis E. Kay[a,b,c,d,2]

Electrostatic interactions and charge balance are important for the formation of biomolecular condensates involving proteins and nucleic acids. However, a detailed, atomistic picture of the charge distribution around proteins during the phase-separation process is lacking. Here, we use solution NMR spectroscopy to measure residue-specific near-surface electrostatic potentials (ϕ_{ENS}) of the positively charged carboxyl-terminal intrinsically disordered 103 residues of CAPRIN1, an RNA-binding protein localized to membraneless organelles playing an important role in messenger RNA (mRNA) storage and translation. Measured ϕ_{ENS} values have been mapped along the adenosine triphosphate (ATP)–induced phase-separation trajectory. In the absence of ATP, ϕ_{ENS} values for the mixed state of CAPRIN1 are positive and large and progressively decrease as ATP is added. This is coupled to increasing interchain interactions, particularly between aromatic-rich and arginine-rich regions of the protein. Upon phase separation, CAPRIN1 molecules in the condensed phase are neutral ($\phi_{ENS} \approx 0$ mV), with ~five molecules of ATP associated with each CAPRIN1 chain. Increasing the ATP concentration further inverts the CAPRIN1 electrostatic potential, so that molecules become negatively charged, especially in aromatic-rich regions, leading to re-entrance into a mixed phase. Our results collectively show that a subtle balance between electrostatic repulsion and interchain attractive interactions regulates CAPRIN1 phase separation and provides insight into how nucleotides, such as ATP, can induce formation of and subsequently dissolve protein condensates.

biomolecular condensates | intrinsically disordered proteins | solution NMR | paramagnetic relaxation enhancement | ATP

Electrostatic interactions play important roles in regulating a plethora of different biochemical processes and in providing stability to biomolecules and their complexes (1–4). As such, the calculation of electrostatic potentials, using Poisson–Boltzmann theory and a high-resolution structure of the molecule of interest (4, 5), has become a powerful tool for understanding enzymatic activity, molecular recognition, and biomolecular interactions, for example, and in the design of inhibitors and activators of molecular function (4, 6, 7). Recent exciting advances in NMR spectroscopy (8, 9) provide an avenue for the de novo experimental determination of near-surface electrostatic potentials in biomolecules with atomic resolution (ϕ_{ENS}) and under a wide range of ionic strengths and solvent conditions (9, 10). These experiments are based on comparing contributions to transverse relaxation of NMR probes, such as protons in the macromolecule studied, from added water-soluble paramagnetic compounds with different charges. Notably, this approach does not a priori require atomic-level structural information, unlike the case for computations. Applications of the NMR technology to small folded proteins, such as ubiquitin, and the Antp homeodomain in complex with a 15-base-pair DNA, have been reported, demonstrating the power of the method and validating theoretical calculations in these cases (9, 10).

Our interest in these experiments lies in applications to intrinsically disordered proteins (IDPs) and to intrinsically disordered regions (IDRs) of proteins, collectively referred to as IDPs in what follows. It is estimated that ~30% of residues within human proteins encode regions of disorder, comprising at least 30 amino acids (11), with many of these proteins playing critical roles in cellular function (12–14), including modulating the formation of membraneless biomolecular condensates that organize proteins and/or nucleic acids, along with a variety of small molecules to regulate biochemical processes in the cell (11, 15, 16). At least 75% of IDPs contain both positively and negatively charged residues (17, 18), with charge–charge interactions important in defining their physical and chemical properties (17, 19) and, in some cases, their propensities to phase separate (20–22). IDPs that interact closely with RNA

Significance

The surface charges of biomolecules can significantly affect how they interact with each other, including, in some cases, whether they can undergo phase separation. One example is the RNA-binding protein CAPRIN1, an important component in membraneless organelles involved in RNA processing. Focusing on the C-terminal intrinsically disordered, positively charged region of CAPRIN1, we have mapped at a residue-specific level the role of electrostatics in phase separation promoted by the addition of adenosine triphosphate. We show that the propensity of CAPRIN1 to form condensates is coupled to its neutralization and formation of intermolecular contacts. Our results highlight the interplay between repulsive electrostatic forces and favorable interchain interactions in regulating the formation of CAPRIN1 condensates.

[1]Y.T. and A.K.R. contributed equally to this work.

[2]To whom correspondence may be addressed. Email: yuki.toyama@utoronto.ca or kay@pound.med.utoronto.ca.

partners are often net positively charged, with many containing RGG/RG motifs that promote phase separation through contacts with oppositely charged RNA molecules (21). One such example is the C-terminal 103-amino-acid region of the CAPRIN1 protein that has been shown to phase-separate in previous studies (23). CAPRIN1 is found in membraneless organelles, such as stress granules, P bodies, and messenger RNA (mRNA) transport granules, where, in concert with a variety of other RNA-binding proteins, it plays an important role in regulating RNA processing (24, 25). The primary sequence of this C-terminal, low-complexity, phase-separating region of CAPRIN1 (hereafter referred to as CAPRIN1) is divided into Arg-rich regions close to the N and C termini and a middle region that is depleted in arginines, but rich in aromatic residues (Fig. 1A and *SI Appendix,* Fig. S1). CAPRIN1 has 15 Arg residues, a pI of 11.5, and a charge of +13 at physiological pH. Not surprisingly, therefore, phase separation requires the addition of salt to screen unfavorable electrostatic interactions (23, 26, 27); alternatively, it can be promoted by adding negatively charged molecules, such as adenosine triphosphate (ATP) or RNA, to a CAPRIN1 solution (23, 27). In what follows, we refer to a phase-separated sample as "demixed" and the phases of low and high protein concentration as "dilute" and "condensed," respectively. In contrast, a single-phase sample (i.e., no phase separation) is "mixed."

With the availability of methods for measuring near-surface electrostatic potentials of proteins, it is now possible to establish quantitatively the important role of electrostatics in controlling the phase separation of CAPRIN1, by monitoring how ϕ_{ENS} "evolves" during the phase-separation process. For example, our previous studies quantifying intermolecular contacts between CAPRIN1 chains using the nuclear Overhauser effect (NOE) had established the important roles of aromatic, Arg, and backbone interactions in stabilizing the condensed phase (27). As phase separation involves a balancing act between these favorable contacts and repulsive like-charge electrostatic interactions, we wondered how ϕ_{ENS} would vary as the propensity for CAPRIN1 to phase-separate increases via the addition of increasing concentrations of ATP ([ATP]). For example, do the positively charged CAPRIN1 chains become fully neutral in the condensed phase, or are favorable interchain interactions sufficient to promote phase separation of only partially neutralized molecules? What is the electrostatic potential when ATP is added to the point where the condensate dissolves? At each stage in the process, how does the charge distribution vary in different regions of CAPRIN1? In order to address these questions, per-residue values of ϕ_{ENS} have been measured by using three water-soluble paramagnetic compounds, with charges of $+1e$, $0e$, and $-1e$, as a function of [ATP], showing a progressive decrease as the ATP concentration increases, leading, ultimately, to phase separation when CAPRIN1 molecules in condensates are neutral ($\phi_{ENS} \approx 0$ mV). Subsequently, upon the addition of sufficient ATP to promote re-entrance to a mixed state (28–30), the electrostatic potential of CAPRIN1 inverts, becoming slightly negative along its primary sequence, likely preventing the close association between
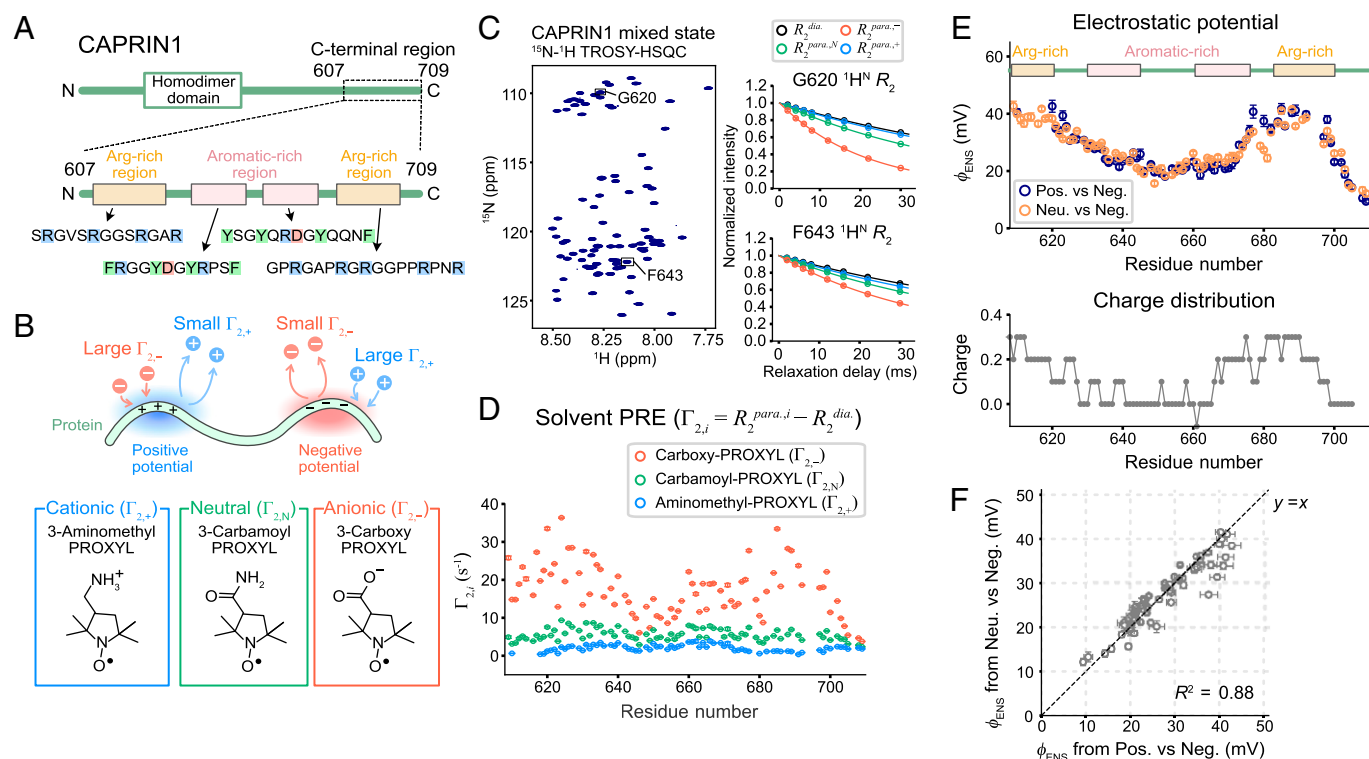
Fig. 1. De novo determination of residue-specific electrostatic potentials of CAPRIN1. (A) Schematic diagram of the C-terminal low-complexity region of CAPRIN1 used in this study. The sequences of the Arg-rich regions (residues 607 to 619 and 682 to 698) and aromatic-rich regions (632 to 643 and 662 to 674) are shown. Positive, negative, and aromatic residues are colored blue, red, and green, respectively. (B) The near-surface electrostatic potential of a charged protein leads to distinct solvent PRE patterns for differently charged paramagnetic cosolutes (indicated by blue, +, and red, −, circles), from which ϕ_{ENS} values are determined (9). The chemical structures of the paramagnetic cosolutes used in this study are shown in B, *Lower*. (C, *Left*) The ^{1}H-^{15}N TROSY HSQC spectrum of CAPRIN1. (C, *Right*) The ^{1}H signal-decay curves for G620 and F643 in the absence or presence of various paramagnetic cosolutes are highlighted. (D) Plots of the solvent ^{1}H^N R_2 PREs from the negative 3-carboxy-PROXYL (red), neutral 3-carbamoyl-PROXYL (green), and positive 3-aminomethyl-PROXYL (blue) are shown. (E) Plots of ϕ_{ENS} potential values of CAPRIN1 determined by using either 3-aminomethyl-PROXYL and 3-carboxy-PROXYL (navy) or 3-carbamoyl-PROXYL and 3-carboxy-PROXYL (orange) cosolutes are shown. The charge vs. residue profile for CAPRIN1 is shown in E, *Lower*, calculated by averaging charge over a sliding window size of 10 residues. Neg., negative; neu., neutral; pos., positive. (F) Correlation plot of the electrostatic potentials obtained by two different pairs of PROXYL derivatives, as shown in E. R^2 is Pearson's correlation coefficient squared. NMR data in C–E were acquired by using 300 μM samples of CAPRIN1, 25 mM MES–NaOH, 3% D$_2$O/97% H$_2$O, pH 5.5, 25 °C at 1 GHz.

molecules that is required for phase separation. Thus, our results paint a picture whereby surface electrostatics play a critical role in regulating CAPRIN1 condensate formation, with condensates comprising neutral CAPRIN1 molecules, so as to eliminate electrostatic repulsion between proximal chains and to allow favorable interchain interactions to dominate.

Results

De Novo Determination of Per-Residue Surface Electrostatic Potentials of Proteins. It has recently been demonstrated that solution NMR spectroscopy can be used to measure ϕ_{ENS} at each backbone amide (9), $^1H^\alpha$, or methyl (10) position of a protein via solvent paramagnetic relaxation enhancements (PREs) of proton magnetization resulting from the addition of differently charged paramagnetic cosolutes with similar chemical structures to the system of interest. This is illustrated schematically in Fig. 1B, where solvent PREs from the positively or negatively charged 2,2,5,5-tetramethylpyrrolidine-N-oxyl nitroxide (PROXYL) derivatives, 3-aminomethyl-PROXYL and 3-carboxy-PROXYL, respectively, are measured. The PRE effect is proportional to the inverse sixth power of the distance between the nitroxide electron and the NMR spin probe—i.e., the local concentration of the spin label, which, in turn, depends on the surface electrostatic potential of the macromolecule studied. Thus, measurement of PREs for a pair of differently charged cosolutes provides an avenue for the determination of per-residue ϕ_{ENS} values, via the relation

$$\phi_{ENS} = -\frac{k_B T}{2e}\ln(\Gamma_{2,+}/\Gamma_{2,-}), \qquad [1]$$

where $2e$ is the charge difference between 3-aminomethyl-PROXYL ($+1e$) and 3-carboxy-PROXYL ($-1e$), k_B is Boltzmann's constant, T is the absolute temperature, and $\Gamma_{2,i}$ $i \in \{+, -\}$ is the R_2 PRE rate for a given proton measured from either the + or − spin label (9). $\Gamma_{2,i}$ values also depend on the total concentration of the added spin label, as well as the correlation time (τ_C) for the interaction between the electron and nuclear dipoles attached to the spin label and macromolecule, respectively (8, 9). It is, therefore, important that the amount of added PRE cosolute be quantified carefully, as described by Yu et al. (9) for dilute solutions of proteins and in *Materials and Methods* for the case of the condensed protein phase. Iwahara and coworkers (9, 10) have measured translational diffusion of positively and negatively charged cosolutes in their original studies to query whether the dipole–dipole correlation time is the same for both molecules. When diffusion values are equal, it is assumed that the ratio of measured PRE rates, which determines ϕ_{ENS} values via Eq. 1 (9), is independent of τ_C, although it is noteworthy that the bulk diffusion constants measured may not report directly on the relevant dynamics at the surface of the protein. In addition to measuring diffusion of paramagetic cosolutes in support of the validity of Eq. 1 for the systems described here (*SI Appendix,* Table S1), we have cross-validated our results from 3-aminomethyl-PROXYL and 3-carboxy-PROXYL by including data obtained with the neutral PROXYL derivative (3-carbamoyl-PROXYL) (8) (Fig. 1B). Agreement between ϕ_{ENS} values calculated from PREs obtained from different pairs of spin labels provides confirmation that potential differences in spin-label concentrations between samples have been properly taken into account and, further, supports the assumption that τ_C values for different cosolutes are similar (see below).

Application to CAPRIN1. As a first step toward investigating the role of electrostatics in the phase separation of CAPRIN1, we determined ϕ_{ENS} values in the mixed state [25 mM 2-(N-morpholino)ethanesulfonic acid (MES)–NaOH, pH 5.5, 25 °C]. The absence of ATP and the very low salt concentration ensures that CAPRIN1 does not phase-separate under these conditions. As reported in our previous studies, N623–G624 and N630–G631 slowly form isoaspartate (IsoAsp)–Gly peptide linkages over time, which can alter the charge distribution of the CAPRIN1 molecule (26). To abolish IsoAsp formation, we introduced N623T and N630T double mutations and used the double Thr mutant (referred to in what follows as CAPRIN1 unless otherwise specified) in all of the experiments presented below, after confirming that the mutant and wild-type proteins exhibited similar propensities to phase-separate (*SI Appendix,* Fig. S2). We measured transverse relaxation rates (R_2) of main-chain amide protons ($^1H^N$) in four separate CAPRIN1 samples, three of which contain one of the three paramagnetic ("*para.*") PROXYL cosolutes, whose chemical structures are illustrated in Fig. 1B, and one with no cosolute (diamagnetic, "*dia.*"). Fig. 1C shows the ^{15}N-^1H transverse relaxation optimized spectroscopy (TROSY) heteronuclear single quantum coherence (HSQC) spectrum (31) of CAPRIN1 at pH 5.5 and 25 °C, along with representative signal decays, from which ^1H R_2 rates are obtained. In this study, a pH of 5.5 was chosen so as to suppress amide-signal broadening due to the rapid solvent exchange that typically occurs in IDPs at more neutral pH values; CAPRIN1 lacks His residues, so that ϕ_{ENS} values are expected to be independent of pH over a range from 5 to well above neutral, and this has been verified by using $^1H^\alpha$-based PRE rates, measured by using a slightly modified version of the haCONHA scheme previously developed (26). The measured signal intensities were fit to a single exponential decay function to obtain ^1H R_2 rates, and the R_2 PRE contributions from three PROXYL derivatives ($\Gamma_{2,i}$, $i \in \{+, N, -\}$, where "+", "N", and "−" denote 3-aminomethyl-PROXYL, 3-carbamoyl-PROXYL, and 3-carboxy-PROXYL compounds, respectively) were calculated from the difference between $^1H^N$ R_2 values measured in the presence ($R_2^{para.,i}$) and absence ($R_2^{dia.}$) of paramagnetic cosolutes ($\Gamma_{2,i} = R_2^{para.,i} - R_2^{dia.}$) (Fig. 1D).

Using the measured PRE rates, initially from 3-aminomethyl-PROXYL ($\Gamma_{2,+}$) and 3-carboxy-PROXYL ($\Gamma_{2,-}$), ϕ_{ENS} values were determined for individual residues in CAPRIN1 (Eq. 1). Fig. 1E (navy) shows the resulting residue-specific ϕ_{ENS} profile. For comparison, the charge distribution predicted from the amino acid sequence is shown below the plot, calculated by using a sliding window of 10 residues with Asp/Glu and Lys/Arg assigned charges of −1 and +1, respectively. As expected from the presence of Arg clusters near the N and C termini, large and positive ϕ_{ENS} potentials (up to +40 mV) were observed in these regions. Intriguingly, a positive potential of approximately +20 mV was measured in the aromatic-rich regions of CAPRIN1, even though the net charge in this central portion of the protein is small (ranging from +1 to +3, depending on the exact boundary conditions used; *SI Appendix,* Fig. S1). The positive potential in the middle section of the protein likely reflects the slight imbalance in charge skewed toward positive as well as the dynamic nature of the CAPRIN1 IDP, whereby the N- and C-terminal Arg-rich regions contact the central portion of the molecule.

CAPRIN1 does not form a stable, folded structure that would allow an accurate prediction of per-residue surface electrostatic potentials so as to cross-validate the experimentally measured values, as has been done in previous studies (9, 10). We, therefore,

adopted an alternative strategy whereby PRE values were also measured by using the neutral 3-carbamoyl-PROXYL cosolute, and ϕ_{ENS} potentials were subsequently calculated by using different combinations of PROXYL derivatives. Fig. 1 *E* and *F* show that good agreement is obtained between profiles computed from Γ_+/Γ_- (navy) and Γ_N/Γ_- (orange; note that $2e$ is replaced by $1e$ in Eq. **1**) combinations (rmsd of 2.8 mV), with a similar level of agreement obtained in a comparison of ϕ_{ENS} values calculated from Γ_+/Γ_N and Γ_+/Γ_- (*SI Appendix*, Fig. S3; rmsd = 2.8 mV) and from Γ_+/Γ_N and Γ_N/Γ_- (rmsd = 5.6 mV). The correspondence of the values measured by using the different cosolutes establishes that robust measures of electrostatic potentials for CAPRIN1 were obtained.

Addition of ATP Reduces and Ultimately Inverts the Electrostatic Potential of CAPRIN1. Our previous studies had established that the addition of ATP–Mg to 400 μM CAPRIN1 solutions at 25 °C and pH 7.4 promotes phase separation when concentrations of nucleotide in the approximate range of 2 to 40 mM are added and subsequent reentry into a mixed state at higher concentrations of ATP–Mg (>50 mM) (27). This is consistent with an important role for electrostatics in the phase separation of CAPRIN1 by ATP (and other negatively charged molecules, such as RNA) and has motivated us to investigate how ϕ_{ENS} values change during the process of ATP-promoted CAPRIN1 phase separation. To this end, we repeated the $^1H^N$ relaxation experiments and analysis described in *Application to CAPRIN1* using data recorded on samples at a number of different ATP concentrations. Our experiments were recorded at pH 5.5 to ensure that high-quality amide spectra could be obtained in both mixed- and demixed-state samples, and we chose to work with ATP in the absence of Mg to minimize pyrophosphate hydrolysis rates (32). Turbidity assays (Fig. 2*A*), measuring light scattering that accompanies phase separation, as a function of ATP concentration [pH 5.5, net ATP charge of −3 (33)], showed similar profiles as those obtained for ATP–Mg at pH 7.4 (27), indicating that 0.8 mM ATP promotes CAPRIN1 (300 μM) demixing, while concentrations exceeding ≈60 mM lead to re-entrance into the mixed state under these conditions.

Having established that ATP promotes phase separation of CAPRIN1 at pH 5.5, we measured per-residue ϕ_{ENS} values for CAPRIN1 (300 μM) at a pair of ATP concentrations: 0.8 mM, where ATP initiates phase separation, with CAPRIN1 in a predominantly mixed state; and 90 mM, where CAPRIN1 has re-entered the mixed state after phase separation. Prior to these measurements, we first compared the NMR spectra of CAPRIN1 in the presence of 0.8 mM and 90 mM ATP (Fig. 2*B*). The chemical-shift titrations observed upon the addition of increasing amounts of ATP, especially in the Arg-rich regions, were consistent with our previous observation that ATP interacts preferentially with the Arg-rich sequences of CAPRIN1 (27) and that the affinity is weak. However, since the chemical-shift changes are not only sensitive to surface electrostatics, but also to various effects, such as the direct binding of ATP, it is difficult to use them as even a qualitative monitor of site-specific changes in electrostatic potentials. To this end, ϕ_{ENS} values of CAPRIN1 (300 μM) were measured by using the negative 3-carboxy-PROXYL and the positive 3-aminomethyl-PROXYL derivatives in the presence of 0.8 mM or 90 mM ATP (Fig. 2*C*). We observed a small, but significant, decrease in ϕ_{ENS} by ~10 to 15 mV upon the addition of 0.8 mM ATP, while at 90 mM ATP, the surface potential of CAPRIN1 had inverted, becoming negative. This is clearly seen in Fig. 2*D*, where, in the absence of ATP, PRE rates are larger with the negatively charged 3-carboxy-PROXYL radical

relative to the positive 3-aminomethyl-PROXYL derivative, indicating a positive surface potential, (Fig. 2*D*, compare red and blue in *Upper*), while at a concentration of ATP of 90 mM, the opposite is true (Fig. 2 *D*, *Lower*). We have also measured ϕ_{ENS} values for a re-entrant solution, where the concentration of ATP is 65 mM (i.e., close to the minimum ATP concentration required to dissolve the condensate) and observed negative surface electrostatic potentials, as for 90 mM ATP (*SI Appendix*, Fig. S4).

The ϕ_{ENS} profile at 0.8 mM ATP (Fig. 2*C*, blue) shows high potential values, especially in the Arg-rich regions (+30 mV). The positive values measured are not surprising, considering that CAPRIN1 and ATP have charges of +13 and −3 per molecule, respectively (pH 5.5), and the ratio of ATP/CAPRIN1 = 0.8 (mM)/0.3 (mM) ≈ 2.7 is not sufficient to neutralize CAPRIN1. We then measured the surface electrostatic potential of a sample comprising 50 μM CAPRIN1 and 0.8 mM ATP, corresponding to a ratio of ATP/CAPRIN1 of ~16 (Fig. 2*C*, yellow). As expected, ϕ_{ENS} values decreased further, although they were all positive, with larger values associated with the arginine-rich regions, as before. Only at several-hundred-fold excess concentration of ATP over protein does the potential become negative (for example, 300:1 in the orange profile of Fig. 2*C*), consistent with very weak interactions between nucleotide and CAPRIN1 and, therefore, rapid exchange between ATP-bound and free states.

Note that while the turbidity assays of Fig. 2*A* establish that condensate formation begins when the concentration of ATP exceeds ~0.8 mM for a concentration of CAPRIN1 of 300 μM, as discussed above, the relatively high ϕ_{ENS} values measured at 0.8 mM ATP (Fig. 2*C*) do not reflect the threshold potentials required for phase separation. Under the conditions of our experiments, the great majority of the NMR signal derives from the dilute phase, as the small droplets of the condensed phase sink to the bottom of the NMR tube and are therefore not detected. Below, we describe a strategy for measuring per-residue ϕ_{ENS} values of molecules in the condensed CAPRIN1 phase and the results of these experiments.

Neutral Electrostatic Potential of the Condensed Phase of CAPRIN1. Fig. 2*C* shows a decrease in ϕ_{ENS} along the trajectory toward phase separation (i.e., increase in ATP concentration). We were interested in establishing what the surface electrostatic potential is for CAPRIN1 in the condensed phase of the demixed state, as the experiments recorded on the mixed-state CAPRIN1 sample (Fig. 2) suggest that, while ϕ_{ENS} must be small, values that are slightly positive, slightly negative, or completely neutral would be possible. An ATP-induced demixed sample was prepared by using a bulk concentration of 3 mM ATP, as described in *Materials and Methods*, with two distinct liquid phases (Fig. 3 *A*, *Right*), including a CAPRIN1-depleted phase on top (dilute phase; 201 μM protein and 2.6 mM ATP) and a CAPRIN1-concentrated phase on the bottom (condensed phase; 33 mM protein and 162 mM ATP) (see *Materials and Methods*). Since the bottom phase covers the radiofrequency coil for NMR signal detection, signals from the protein-condensed phase could be selectively observed, and the per-residue electrostatic potential of the CAPRIN1 condensate could, therefore, be measured.

Fig. 3*A* shows the ^{15}N-^1H TROSY HSQC spectrum of CAPRIN1 in the condensed phase recorded by using a sample containing 2% ^2H,^{15}N-labeled protein in an unlabeled CAPRIN1 background (25 mM MES–NaOH, pH 5.5 and 40 °C). Deuteration leads to significant gains in both spectral sensitivity and resolution, as a result of the elimination of a multitude of ^1H-^1H dipole–dipole interactions, which is especially important in the
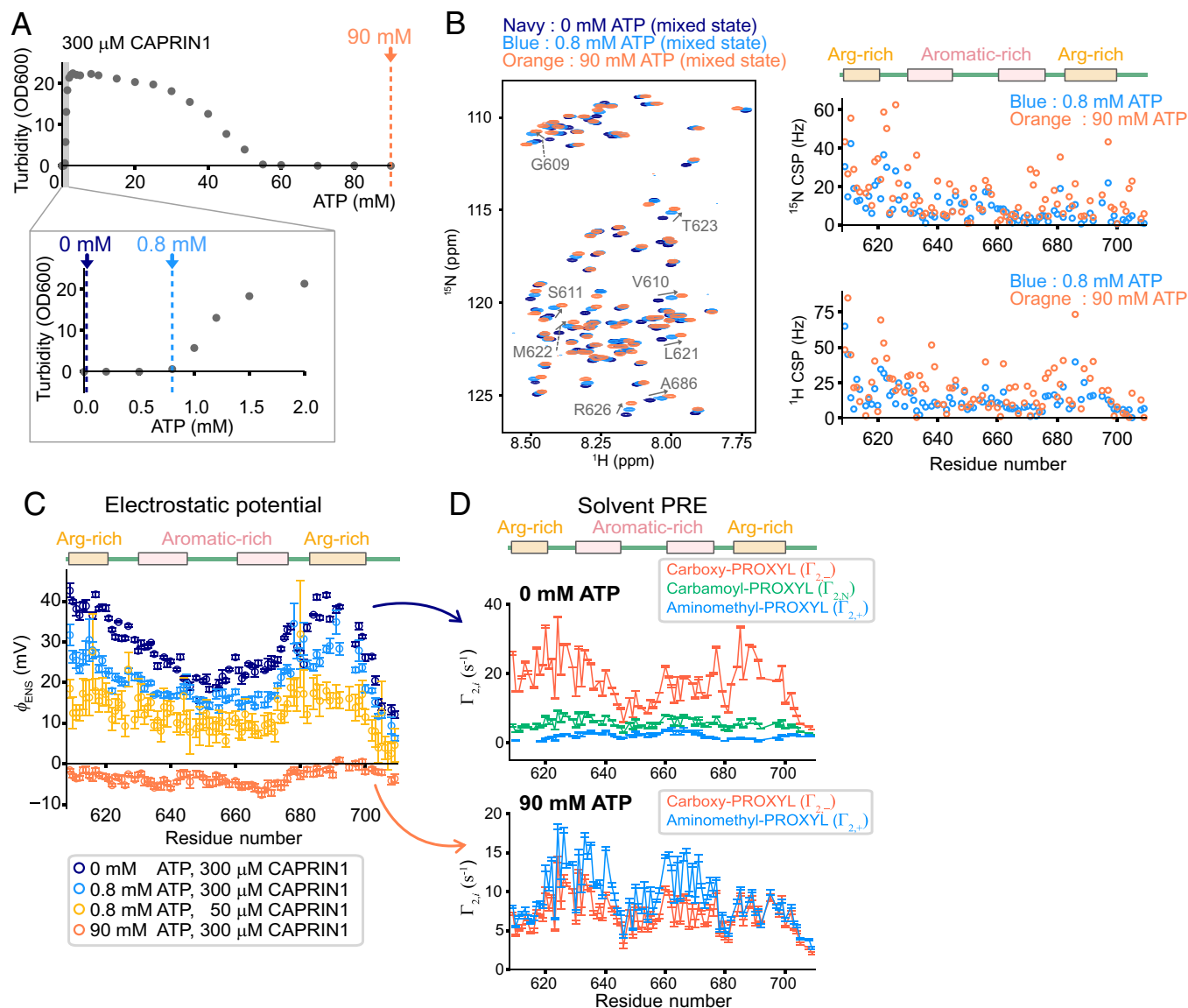
Fig. 2. Effect of ATP on CAPRIN1 ϕ_{ENS} potentials. (*A*) Turbidity assays measuring phase-separation propensities of 300 μM samples of CAPRIN1 as a function of [ATP], 25 mM MES–NaOH, pH 5.5. The vertical dotted lines indicate the data points with 0 mM (navy), 0.8 mM (blue), or 90 mM (orange) ATP used in the NMR experiments. (*B, Left*) Overlay of ^{15}N-^{1}H TROSY HSQC spectra measured in the presence of 0 mM (navy), 0.8 mM (blue), and 90 mM (orange) ATP. (*B, Right*) Plots of the ^{15}N (*Upper*) or ^{1}H (*Lower*) chemical-shift differences (absolute values) upon the addition of 0.8 mM (blue) or 90 mM (orange) ATP. (*C*) Plots of ϕ_{ENS} values measured with 0 mM (navy), 0.8 mM (blue), and 90 mM (orange) ATP using 300 μM samples of CAPRIN1. A plot of ϕ_{ENS} measured with 0.8 mM ATP and a 50 μM sample of CAPRIN1 is also shown (yellow). ϕ_{ENS} potentials were determined by using 3-carbamoyl-PROXYL and 3-carboxy-PROXYL for the 0 mM ATP dataset or by using 3-carboxy-PROXYL and 3-aminomethyl-PROXYL for the 0.8 mM and 90 mM ATP datasets. (*D*) Plots of solvent ^{1}H^{N} R_2 PRE rates from negative 3-carboxy-PROXYL (red), neutral 3-carbamoyl-PROXYL (green), and positive 3-aminomethyl-PROXYL (blue) radicals in the absence (*Upper*) and presence (*Lower*) of 90 mM ATP. NMR data in *B–D* were acquired by using 300 μM or 50 μM samples of CAPRIN1, 25 mM MES–NaOH, 3% D_2O/97% H_2O, pH 5.5, 25 °C at 1 GHz. Errors in *A* were obtained from triplicate measurements (smaller than data points), and those in *C* and *D* were obtained by propagating the error in R_2.

condensed phase, where molecules tumble much more slowly than in the mixed state (27). As the spectral quality of CAPRIN1 in the condensed phase improves with temperature, all of our experiments on condensates were performed at 40 °C (27), where it is possible to measure residue-specific ^{1}H R_2 rates for the majority of the backbone amides (70 of 92 possible amide signals; Fig. 3 *A, Right*) in separate samples doped with the three different PROXYL derivatives, from which solvent PREs were obtained. Small differences in concentration of the paramagnetic cosolutes in the condensed-phase samples were carefully taken into account, based on a set of R_1 PRE measurements of water and an internal standard molecule, fluorodeoxyglucose, recorded on the same samples used to measure ϕ_{ENS} values (see *Materials and Methods* and *SI Appendix*, Fig. S5 for details). The solvent PREs were very

similar between the positive, neutral, and negative PROXYL derivatives across the protein (Fig. 3*B*), indicating that the surface potential of CAPRIN1 in the condensed phase was close to neutral at each site (Fig. 3*C*). ϕ_{ENS} values calculated from different pairs of PROXYL derivatives—for example, the positive 3-aminomethyl-PROXYL ($\Gamma_{2,+}$) vs. the negative 3-carboxy-PROXYL ($\Gamma_{2,-}$) or the neutral 3-carbamoyl-PROXYL ($\Gamma_{2,N}$) vs. the negative 3-carboxy-PROXYL ($\Gamma_{2,-}$) compounds—were in good agreement (Fig. 3*C*), providing a high level of confidence in the measurements. Thus, charge neutralization is a prerequisite for forming a stable CAPRIN1 condensed phase, at least when prepared with a bulk ATP concentration of 3 mM, as done here.

As CAPRIN1 is neutral under these conditions, it is expected that each molecule would be surrounded by a sufficient number
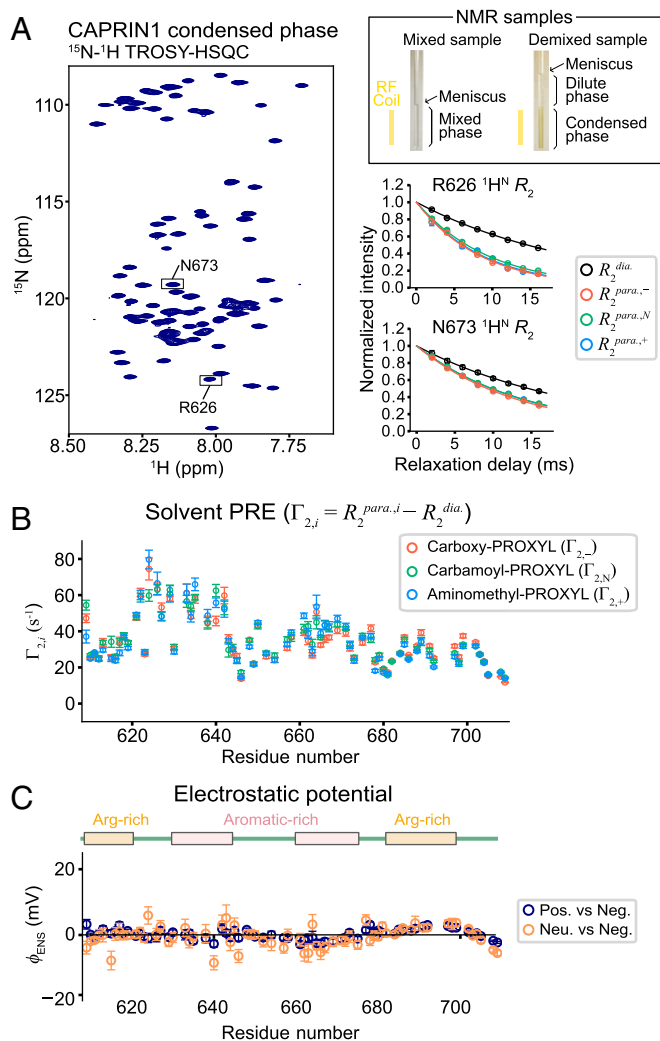
Fig. 3. CAPRIN1 is neutral in the condensed phase. (*A, Left*) The ^{15}N-^{1}H TROSY HSQC spectrum of a condensed-phase CAPRIN1 sample (162 ± 6.9 mM ATP and 32.9 ± 1.7 mM protein). (*A, Right*) The ^{1}H^N signal-decay curves for R626 and N673 in the absence or presence of various paramagnetic cosolutes are shown. NMR sample tubes containing mixed-state (left) or demixed-state (right) samples are shown in A, *Right Upper*. (*B*) Plots of ^{1}H^N solvent R_2 PREs from the negative 3-carboxy-PROXYL (red), neutral 3-carbamoyl-PROXYL (green), and positive 3-aminomethyl-PROXYL (blue) cosolutes are shown. The $\Gamma_{2,N}$ and $\Gamma_{2,-}$ values were scaled so that the concentrations of paramagnetic cosolutes are the same as that in the 3-aminomethyl-PROXYL dataset, as described in *Materials and Methods*. (*C*) CAPRIN1 ϕ_{ENS} potentials determined by using 3-aminomethyl-PROXYL and 3-carboxy-PROXYL (navy) or 3-carbamoyl-PROXYL and 3-carboxy-PROXYL (orange). All NMR measurements were performed on a condensed-phase sample, 25 mM MES–NaOH, 10% D$_2$O/90% H$_2$O, pH 5.5, 40 °C, 1 GHz. Error bars in *B* and *C* were determined by propagating errors in R_2 rates. Neg., negative; neu., neutral; pos., positive.

of ATPs, so as to balance charge (+13 for CAPRIN1). Since at pH 5.5, the charge of each ATP is −3, a simple prediction is that at least $13/3 = 4.3$ molecules of ATP are required for each copy of the protein. As the affinity of ATP for CAPRIN1 is weak, it is likely that 4.3 is a lower bound. To test this, we have measured the concentrations of ATP and CAPRIN1 inside condensates (*Materials and Methods*), obtaining 162 ± 6.9 mM and 32.9 ± 1.7 mM, respectively, and yielding the ratio, [ATP]/[CAPRIN1] = 4.9, in reasonable agreement with the predicted value of 4.3 based on charge neutrality.

Correspondence between Reduced Electrostatic Potential and Intermolecular CAPRIN1 Interactions. We hypothesized that intermolecular contacts between CAPRIN1 chains would concomitantly strengthen along the trajectory toward phase separation by the addition of ATP, as the electrostic potential of CAPRIN1 decreases, leading to less electrostatic repulsion between proximal molecules. To characterize intermolecular interactions between CAPRIN1 chains, we performed an intermolecular PRE experiment, in which a spin label was covalently attached to one half of the molecules (not isotopically labeled) and the effects on the spectra of ^{13}C,^{15}N-labeled molecules in the sample were quantified (Fig. 4*A*). Spin labels were introduced by making single Cys mutations (S615C, A658C, and S678C) (Fig. 4*B*) and modification of the resultant Cys side chain through the addition of the 2,2,6,6-tetramethyl-1-piperidinyloxy radical (TEMPO). The positions chosen (615, 658, and 678) correspond to the Arg-rich region near the N terminus (615), proximal to the C-terminal Arg region (678), or to the middle aromatic-rich sequence (658) of CAPRIN1. After confirming that the introduction of TEMPO did not significantly perturb the phase-separation propensities of the modified CAPRIN1 molecules (Fig. 4*C*), intermolecular PREs were quantified from differences in the ^{1}H R_2 rates measured for the paramagnetic and diamagnetic samples comprising 150 μM ^{13}C,^{15}N CAPRIN1 and 150 μM TEMPO-labeled/NMR-unlabeled CAPRIN1 (TEMPO was reduced by adding ascorbate in the diamagnetic sample). The measurements were also performed in the presence of 0.8 mM ATP, where CAPRIN1 starts to phase-separate, and at 90 mM ATP, where the ϕ_{ENS} distribution is slightly negative (Fig. 2*C*).

Fig. 4*D* illustrates the intermolecular PRE patterns from three spin-labeled positions measured in the presence of either 0.8 or 90 mM ATP or in the absence of ATP altogether (mixed samples). The interpretation of PRE values is complicated by the fact that they depend on both the distance between the spin label on one chain and the amide proton on a neighboring chain (whose R_2 is measured) and the dynamics of the vector connecting the electron and proton dipoles. Nevertheless, increased PRE values as a function of ATP can, qualitatively, be interpreted to indicate that the spin label of one chain becomes "closer" to a second chain at the position(s) where the PREs grow. In the absence of ATP, no significant intermolecular PREs were observed in all cases, consistent with contacts between CAPRIN1 chains being largely suppressed by electrostatic repulsion between the positively charged molecules. In contrast, in the presence of 0.8 mM and 90 mM ATP, significant intermolecular PREs were observed. Notably, the intermolecular PREs, and, hence, intermolecular contacts, were largest in the presence of 90 mM ATP, where the surface electrostatic potential is closest to neutral along the backbone of the protein (−3.4 mV, on average) and decreased as the surface charge increased (maximum ϕ_{ENS} values of +40 mV and + 30 mV for samples with 0 mM and 0.8 mM ATP, respectively).

The PREs from each spin label show similar profiles, with increased values mainly in the aromatic-rich portions of the molecule, consistent with our previous intermolecular NOE analyses showing a number of interaction hotspots (residues 624 to 626, 638 to 640, and 660 to 666) localized to these aromatic-rich regions (27). The magnitudes of the PREs follow the order: A658C (aromatic-rich region) > S615C (N-terminal Arg-rich region) > S678C (close to the C-terminal Arg-rich region), with the PREs from the A658C and S615C sites being quite similar in magnitude. This underscores that intermolecular interactions are degenerate in the condensed state, with similar contacts involving the three probes to neighboring CAPRIN1 chains. Thus, intermolecular interactions are formed between the aromatic-rich regions and also between the
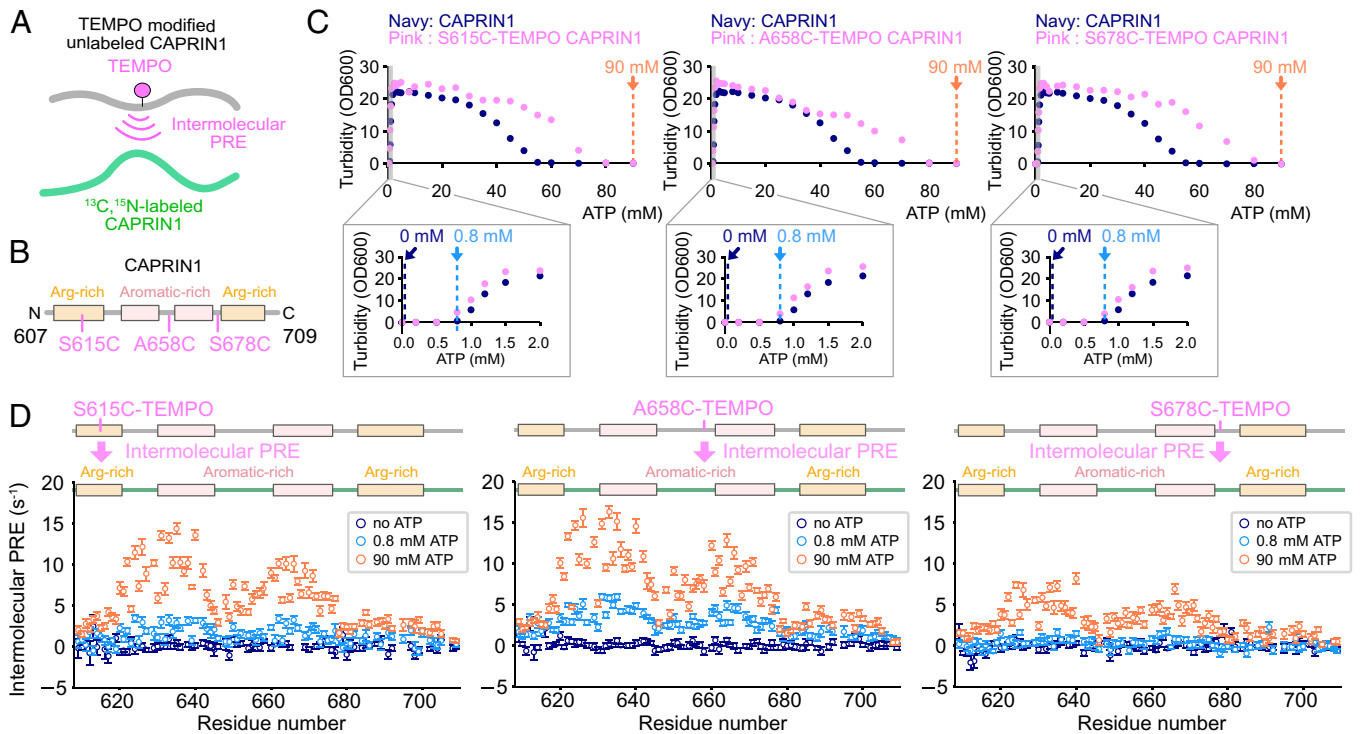
Fig. 4. Intermolecular contacts increase as electrostatic potential decreases in mixed-state CAPRIN1 samples. (*A*) Schematic of the sample composition used to measure the intermolecular PRE effect. (*B*) The positions of the Cys mutations in the intermolecular PRE experiments (one at a time), and, hence, the spin labels, are indicated. (*C*) Turbidity assays measuring phase-separation propensities of 300 μM samples of CAPRIN1 (navy) and TEMPO-modified Cys mutant CAPRIN1 (pink) as a function of [ATP] at room temperature. The vertical dashed lines indicate the data points with 0 mM (navy), 0.8 mM (blue), and 90 mM (orange) ATP used in the NMR relaxation experiments for quantifying intermolecular PREs. (*D*) Intermolecular PRE profiles from S615C-TEMPO (*Left*), A658C-TEMPO (*Center*), and S678C-TEMPO (*Right*) samples, 150 μM ^{12}C,^{14}N-TEMPO CAPRIN1 and 150 μM ^{13}C,^{15}N CAPRIN1, 25 mM MES–NaOH, 3% D$_2$O/97% H$_2$O, pH 5.5, are shown. The data recorded without ATP (navy) and with 0.8 mM (blue) and 90 mM (orange) ATP are overlaid in each plot. Errors in *C* were obtained from triplicate measurements (smaller than the data points), while those in *D* were obtained by propagating the errors in R_2 values. All of the data were recorded at 1 GHz, with the exception of the S615C 0 mM and 0.8 mM ATP datasets, measured at 800 MHz, 25 °C.

aromatic-rich and Arg-rich regions of adjacent molecules, with aromatic, arginine, and other residues functioning as stickers that promote phase separation (34), likely including backbone groups, as highlighted in our previous intermolecular NOE study (27). Arg is present in both the aromatic-rich and Arg-rich regions and generally plays important roles in phase separation through the formation of cation–π, π–π, and/or hydrogen-bonding interactions (20, 21, 35, 36), with mutations of Arg to Lys abolishing the ability of CAPRIN1 to phase-separate (26). Notably, larger intermolecular PREs were observed for the N-terminal relative to the C-terminal Arg region, consistent with our previous observations that mutations in the N-terminal Arg-rich region have a bigger effect on CAPRIN1 phase-separation propensity than mutations in the corresponding region at the C terminus (26).

Discussion

Phase separation of biomolecules to form condensates is critical for proper cellular function (15, 37). Thus, the atomic details of the interactions that drive this process, and the subsequent disassembly of protein condensates, are of great interest. There is a growing awareness of the important role of charge–charge interactions in regulating condensate formation, with some biologically relevant phase-separating proteins enriched in charged residues (21). Perturbations to protein electrostatics, often induced by interactions with charged molecules, such as ATP or RNA (28, 38), or resulting from posttranslational modifications (35, 39, 40), can dramatically affect a protein's phase-separation propensity. In these cases, the measurement of

electrostatic surface potentials would provide valuable insight into the phase-separation process, and an understanding of how such potentials are altered along the phase-separation trajectory would result in a more rigorous description of the process of biomolecular condensation.

Here, we have applied a recently developed solution NMR method for the de novo determination of per-residue near-surface electrostatic potentials of proteins (9) to study the ATP-driven phase separation of the C-terminal low-complexity disordered region of CAPRIN1, an RNA-binding protein that is involved in the regulation of mRNA translation and stability (24, 25). Our results establish that, at least in the positively charged CAPRIN1 system, decreases in ϕ_{ENS} upon addition of increasing amounts of ATP correlate with progression toward the phase-separated state, as illustrated schematically in Fig. 5. In the absence of ATP, CAPRIN1 has a positive surface potential across the molecule (more than +20 mV), with maxima at the N- and C-terminal Arg-rich regions of the protein (approximately +40 mV). Thus, electrostatic repulsion of proximal chains prevents self-association (Fig. 5, step I). Notably, a positive potential was measured not only for the N- and C-terminal Arg-rich regions near the termini, but also in the aromatic-rich region (which also contains a number of Arg and Lys residues), where interaction hotspots have been identified in condensed CAPRIN1 samples (27). As the aromatic-rich regions of sequence contain significantly fewer charged residues, the delocalized positive charge in this area, likely resulting from interactions with the more positively charged termini, may prevent intermolecular contacts from occurring between aromatic moieties and other "stickers" (34). Upon the addition of ATP, the
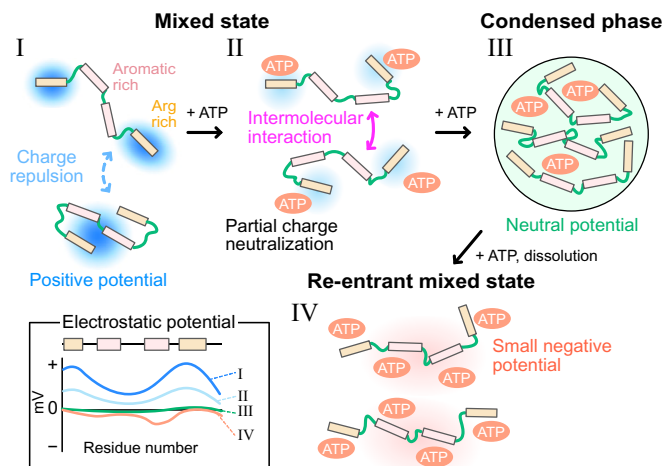
Fig. 5. The electrostatic potential of CAPRIN1 along its ATP-induced phase-separation trajectory. CAPRIN1 has large, positive ϕ_{ENS} values in the absence of ATP (*I*). The addition of ATP decreases its positive potential and promotes intermolecular interactions (*II*). CAPRIN1 condensates are neutral, $\phi_{ENS} \approx 0$ mV (*III*), and further addition of ATP inverts the potential, with negative ϕ_{ENS} values in the aromatic regions, leading to dissolution of the condensed phase and re-entrance into the mixed state (*IV*). A schematic of ϕ_{ENS} for the various ATP concentrations discussed in the text is shown.

positive surface potential of CAPRIN1 decreases, initially more in Arg-rich regions, consistent with results from previous ATP–Mn PRE studies (27), showing that ATP interacts initially with the positively charged termini of the protein (Fig. 5, step II). Increasing amounts of ATP eventually lead to the accumulation of a condensed phase (demixed state) and neutralization of CAPRIN1 chains (Fig. 5, step III), where each protein molecule interacts with ~5 equivalents of ATP (34). Neutralization of CAPRIN1 is accompanied by favorable intermolecular interactions connecting neighboring CAPRIN1 molecules, stabilizing the protein-condensed phase (Fig. 5, step III). Further addition of ATP (>60 mM bulk concentration; Fig. 2A) leads to re-entrance into a mixed phase. This is accompanied by a charge inversion of CAPRIN1, with a slight negative potential localized to the aromatic-rich regions of the molecule, consistent with ATP interactions with these regions that have been observed in ATP–Mn PRE experiments (27). Such interactions may also contribute to ATP's ability to dissolve certain condensates (28). The net negative potential of the CAPRIN1 chain and interactions of ATP with aromatic stickers likely prevent the intermolecular contacts that are required for phase separation, leading to disassembly of condensates (Fig. 5, step IV).

Our intermolecular PRE results show a strong correlation between reduction in electrostatic potential and enhanced intermolecular interactions, supporting the model in Fig. 5 and pointing to a scenario whereby phase separation of CAPRIN1 can be promoted by the addition of any charged molecule that neutralizes or shields its positive potential. For example, it is known that salts, such as sodium chloride, lead to CAPRIN1 phase separation in the absence of other additives (23, 26) and that phosphates, pyrophosphates, RNA, or phosphorylated proteins, such as fragile X mental retardation protein (FMRP), can similarly induce CAPRIN1 phase separation (23, 26). Further, the decrease in net charge by posttranslational modifications also promotes phase separation, as observed for Tyr-phosphorylated CAPRIN1 that condenses at lower concentrations than unmodified protein or under conditions of less added salt (23, 26). CAPRIN1 coexists with negatively charged RNA molecules in cells and, along with FMRP and other proteins, is implicated in the

regulation of RNA processing and translational activity (23, 24). Thus, electrostatics play a central role in modulating the biological functions of this protein, and measurement of electrostatic potentials at each site along its backbone, as reported here, provides an opportunity to understand in more detail the important role of charge in this system. Future applications of these methods (9, 10) will pave the way for mapping the role of electrostatics in phase separation in a more general sense, including the effects of sequence, charge patterning, posttranslational modifications, and the presence of nucleic acids.

Materials and Methods

Sample Preparation. The C-terminal low-complexity region of CAPRIN1 (residues 607 to 709; Uniprot: Q14444) was expressed and purified as described (23, 26). N623T and N630T double mutations and Cys mutations (S615C, A658C, and S678C) were introduced by using Quikchange site-directed mutagenesis (Agilent). Unlabeled proteins were expressed for 4 to 5 h at 37 °C following induction using 0.5 mM isopropyl ß-D-1-thiogalactopyranoside (IPTG) in Terrific Broth medium. Uniformly $^{13}C,^{15}N$-labeled CAPRIN1 was produced by bacterial expression, using minimal medium supplemented with [U-^{13}C]-glucose and $^{15}NH_4Cl$ as the sole carbon and nitrogen sources, respectively. The protein was expressed after induction with 0.5 mM IPTG at an optical density at 600 nm (OD600) of ~0.6 to 0.8 for 6 h at 37 °C. Uniformly $^2H,^{15}N$-labeled CAPRIN1 was prepared by expression using D$_2$O-based minimal media, supplemented with [U-^{2}H]-glucose and $^{15}NH_4Cl$. The protein was expressed after induction with 0.5 mM IPTG at OD600 ~ 0.6 to 0.8 overnight at 25 °C. The mixed-state NMR samples comprised 50 to 300 μM U-$^{13}C,^{15}N$ CAPRIN1, 25 mM MES–NaOH (pH 5.5), and 3% D$_2$O, with or without 0.8 to 90 mM ATP (Biobasic). The demixed-state samples were prepared as described (23). Briefly, phase separation was induced by mixing 300 μM CAPRIN1, 2% $^2H,^{15}N$-labeled protein + 98% unlabeled protein, with 3 mM ATP in 25 mM MES (pH 5.5) and 10% D$_2$O at room temperature. After centrifugation, the bottom phase, corresponding to the condensed protein, was transferred to a 3-mm NMR tube. For solvent PRE measurements in mixed-state samples, either 3-aminomethyl-PROXYL, 3-carbamoyl-PROXYL, or 3-carboxy-PROXYL (Sigma-Aldrich) was added to a final concentration of 5 mM from ≈100 mM stock solutions. The concentrations of the paramagnetic cosolutes in the stock solutions were measured by ^{1}H one-dimensional (1D) NMR after reducing the spin label, using a procedure established by Iwahara and coworkers (9). For the condensed-phase samples, volumes were estimated after vortexing, and each PROXYL derivative was added to a concentration of ≈5 mM, along with ≈1 mM 2-deoxy-2-fluoro-D-glucose (FDG; FLUKA), before transferring the condensed phase to a 3-mm NMR tube.

Spin-Labeling for Measurement of Intermolecular PREs. Purified Cys-mutant CAPRIN1 was reduced by incubating with 5 mM dithiothreitol (DTT), after which the CAPRIN1 solution was buffer-exchanged into a DTT-free buffer by passing the protein solution through a PD-10 desalting column (Cytiva). Proteins were then incubated with 10 equivalents of *N*-(1-oxyl-2,2,6,6-tetramethyl-4-piperidinyl)maleimide (4-maleimido-TEMPO) (Toronto Research Chemicals) and allowed to react overnight at 4 °C in buffer containing 25 mM sodium phosphate and 2 M guanidinium chloride. The reaction was quenched by adding 5 mM DTT. Unreacted 4-maleimide-TEMPO was removed by a HiPrep 26/10 Desalting column (Cytiva). The reduced state of the spin label was prepared by incubating TEMPO-labeled CAPRIN1 with 20 equivalents of L-ascorbic acid overnight at room temperature. Cys modifications were confirmed by using electrospray-ionization mass spectrometry.

Turbidity Assays. Purified CAPRIN1 samples were diluted to a protein concentration of 300 μM with 25 mM MES–NaOH at pH 5.5, containing varying concentrations of ATP (ranging from 0 to 90 mM). After vigorous mixing, 5-μL samples were loaded into a μCuvette G1.0 (Eppendorf). OD600 measurements were recorded three times by using a BioPhotometer D30 (Eppendorf).

NMR Measurements. All of the ^{1}H-detected NMR measurements were performed at 23.5 Tesla (1-GHz ^{1}H frequency) on a Bruker Avance Neo spectrometer or at 18.8-Tesla (800-MHz ^{1}H frequency) or 14.0-Tesla (600-MHz ^{1}H frequency)

Bruker Avance III HD spectrometers, all equipped with cryogenically cooled x, y, z pulsed-field gradient triple-resonance probes. The ^{19}F-detected NMR measurements were performed at 11.7 Tesla (500-MHz ^{1}H frequency) on a Bruker Avance III HD spectrometer equipped with a liquid nitrogen-cooled z pulsed-field gradient triple-resonance probe. All spectra were processed and analyzed by using the NMRPipe suite of programs (41) and visualized by using the Python package nmrglue (42). Peak intensities were extracted either by using the Peakipy software package (https://github.com/j-brady/peakipy) for two-dimensional datasets or by sum integrations for 1D datasets.

The ^{1}H^N R_2 relaxation measurements were performed by using a TROSY-based pulse scheme (31), with a ^{1}H spin-echo variable delay interval inserted immediately prior to direct detection. A selective REBURP pulse (43) (length of 1,800 μs and centered at 7.7 ppm, 1 GHz) was applied in the center of the ^{1}H spin-echo relaxation element, which refocuses homonuclear J-evolution from scalar couplings between ^{1}H^N and aliphatic proton spins. The measurements were performed at 1 GHz or 800 MHz at 25 °C for the mixed-state samples and 1 GHz at 40 °C for the demixed-state samples. The ^{1}H^N PREs were quantified by fitting the decay of signals to a single exponential function to obtain $R_2^{para,i}$ and $R_2^{dia.}$ rates, from which the PRE contribution was calculated as $\Gamma_{2,i} = R_2^{para,i} - R_2^{dia.}$. Exponential curve fits were performed by using in-house-written programs (Python 3.7), exploiting the Levenberg–Marquardt algorithm of the Lmfit python software package (https://lmfit.github.io/lmfit-py/). Uncertainties in R_2 were computed as the SEs of the fit.

Water ^{1}H R_1 or FDG ^{19}F R_1 rates were measured by using a saturation-recovery scheme, in which signal was initially eliminated prior to a variable-length recovery delay. The water ^{1}H R_1 rate was measured at 600 MHz and 40 °C with signal readout using an excitation pulse with a small flip angle (<15°). The ^{19}F R_1 of FDG was measured at 500 MHz and 40 °C by using a triple-pulse excitation-scheme readout to suppress the residual ^{19}F background in the probe, as well as radiofrequency acoustic ringing (44). R_1 rates were obtained by fitting the recovery of signals to the equation $I(t) = I_{eq.}(1 - e^{-R_1 t})$, where I(t) is the signal intensity at time t, and $I_{eq.}$ is the signal intensity at thermal equilibrium, using in-house-written programs. Uncertainties in R_1 were computed as the SEs of the fits.

The diffusion constants of PROXYL derivatives in the reduced form (reduced via addition of 10 mM ascorbic acid for at least 1 h, 37 °C) were measured by using stimulated echo longitudinal encode-decode experiments with bipolar gradients to encode and decode magnetization, along with watergate solvent suppression (600 MHz, 25 °C) (45, 46). The samples contained 25 mM MES–NaOH (pH 5.5), 5 mM PROXYL derivatives, 10 mM ascorbic acid, and 3% D$_2$O/97% H$_2$O. Uncertainties in diffusion constants were calculated as SEs in the fits.

Calculations of Near-Surface Electrostatic Potentials. Near-surface electrostatic potentials were calculated from the R_2 PRE rates obtained with a pair of PROXYL derivatives ($\Gamma_{2,i}$ and $\Gamma_{2,j}$) using the following equation as described (9):

$$\phi_{ENS} = -\frac{k_B T}{\Delta e}\ln(\Gamma_{2,i}/\Gamma_{2,j}), \qquad [2]$$

where $k_B = 8.62 \times 10^{-5}$ eV/K; $T = 298.15$ K for the mixed-state samples and 313.15 K for the demixed state samples; e is the charge of an electron; and Δ is the charge difference between i and j PROXYL derivatives (for example, $\Delta = 2$ for $\{i, j\} = \{+, -\}$ and $\Delta = 1$ for $\{i, j\} = \{N, -\}$). In the calculations, only residues with PREs larger than 0.5 s^{-1} were used. Eq. **2** assumes that the concentration of the two paramagnetic cosolutes (i and j) are the same, which can be easily achieved in the mixed-state samples (9). In the demixed-state samples, however, the concentrations of cosolutes in the condensed phase could be different from the bulk concentration. It is possible that cosolute molecules partition differently into the dilute and condensed phases of the demixed-state sample, given the differences in the charge of each PROXYL derivative. To this end, for the demixed-state samples, we corrected the experimental ratio $\Gamma_{2,i}/\Gamma_{2,j}$, denoted by $\Gamma_{2,i}^{corr.}/\Gamma_{2,j}^{corr.}$ below, to take into account potential differences in concentrations of cosolutes. This was achieved by first noting that, like for ^{1}H R_2 PRE rates, R_1 PRE rates are also proportional to the concentration of spin label (8, 9, 47). A separate set of experiments was performed where either ^{1}H (water) or ^{19}F (1 mM FDG) R_1 rates were measured in either buffer or mixed-state CAPRIN1

samples (6 mM protein) in the presence of various concentrations of each PROXYL derivative. The rates were found to be linear as a function of concentration and subsequently fitted to (SI Appendix, Fig. S5)

$$R_{1,i}(c) = k_i c + R_{1,i}(0), \qquad [3]$$

where c is the concentration of the paramagnetic cosolute and $R_{1,i}(c)$ is the R_1 rate of the probe signal at a concentration of c. In the case of water, the values of k_i differed by 10 to 20% between the three PROXYL derivatives, presumably reflecting small differences in contact distances between water and paramagnetic cosolutes. The k_i values for FDG were almost identical. After establishing a set of "calibration curves" (SI Appendix, Fig. S5), $\Gamma_{2,i}^{corr.}/\Gamma_{2,j}^{corr.}$ ratios were calculated as

$$\frac{\Gamma_{2,i}^{corr.}}{\Gamma_{2,j}^{corr.}} = \frac{\Gamma_{2,i}^{exp.}}{\Gamma_{2,j}^{exp.}} \cdot \frac{\Gamma_{1,j}}{\Gamma_{1,i}} \cdot \frac{k_i}{k_j}, \qquad [4]$$

where $\Gamma_{2,i}^{exp.}$ and $\Gamma_{2,j}^{exp.}$ are experimentally measured ^{1}H^N R_2 PRE values, and $\Gamma_{1,i}$ and $\Gamma_{1,j}$ are the water or FDG R_1 PRE rates (i.e., $\Gamma_{1,i} = R_1^{para.,i} - R_1^{dia.}$, which is proportional to the concentration of the spin label) measured in the condensed-phase sample. The product $\frac{\Gamma_{1,j}}{\Gamma_{1,i}} \cdot \frac{k_i}{k_j}$ corrects for differences in concentrations of cosolutes in each sample, with the ratio of k values taking into account that, at least for water, the R_1 PRE rates slightly depend on the nature of the spin label, even when they are present at identical concentrations. Errors in ϕ_{ENS} were obtained by propagating errors in R_2 PRE rates.

We confirmed that the corrected R_2 PRE ratios (Eq. **4**) obtained from either water or FDG were consistent. In practice, the ratio of the R_2 PREs ($\Gamma_{2,i}^{corr.}/\Gamma_{2,j}^{corr.}$) differed by only ~10% from the uncorrected ratio, indicating that each of the PROXYL derivatives partitioned similarly into the condensed phase.

As described, all of the NMR experiments were carried out at pH 5.5 to ensure high-quality spectra. Asssuming the reported pK$_a$ value for the carboxy group of the 3-carboxy-PROXYL derivative (pK$_a$ = 3.9 to 4.0) (48), ~97% (3%) of the added 3-carboxy-PROXYL compound would be negatively charged (neutral) at this pH value, leading to less than 1-mV systematic error in the potential values measured when this compound is used, a value typically smaller than the experimental error. Therefore, we did not take into account and correct for the presence of the neutral form of the spin label in any of our analyses.

Measuring the Concentrations of CAPRIN1 and ATP in the Condensed Phase. A condensed-phase sample of CAPRIN1 was prepared by mixing unlabeled CAPRIN1 and ATP at bulk concentrations of 300 μM and 3 mM, respectively, in 25mM MES–NaOH buffer, pH 5.5. The condensed phase was accumulated to get a net volume of ≈150 μL in a PCR tube. The tube was placed in a PCR thermocycler with a heated lid (95 °C) and maintained at 40 °C for ~1 h after vortexing to let the condensed phase settle to the bottom of the tube. Subsequently, 2 μL and 10 μL of the condensed and dilute phases, respectively, were drawn from the sample by using a positive and air-displacement pipette and diluted into the size-exclusion chromatography (SEC) buffer (50 mM Tris·HCl, pH 8.0, 200 mM NaCl, and 3 M guanidinium chloride) to get a net sample volume of 200 μL. Samples were then injected into a 100-μL sample loop and run on a Superdex 75 10/300 GL column (Cytiva) equilibrated in SEC buffer (flow rate of 1 mL/min). Standard curves for ATP and CAPRIN1 were determined in an analogous manner. SEC chromatograms were baseline-corrected by using the ASpecD package in python and integrated to get peak areas used for quantification of the concentrations. Data are reported as the mean and SD of repeated measurements ($n = 6$). Concentrations of {ATP and CAPRIN1} in the condensed and dilute phases are {162 ± 6.9 mM and 32.9 ± 1.7 mM} and {2.6 ± 0.10 mM and 201 ± 35 μM}, respectively.

Data, Materials, and Software Availability. All data are included in the article and/or SI Appendix.

Author affiliations: [a]Department of Molecular Genetics, University of Toronto, Toronto, ON M5S 1A8, Canada; [b]Department of Biochemistry, University of Toronto, Toronto, ON M5S 1A8, Canada; [c]Department of Chemistry, University of Toronto, Toronto, ON M5S 1A8, Canada; and [d]Program in Molecular Medicine, Hospital for Sick Children, Toronto, ON M5G 1X8, Canada

1. M. F. Perutz, Electrostatic effects in proteins. *Science* **201**, 1187–1191 (1978).
2. A. Warshel, Electrostatic basis of structure-function correlation in proteins. *Acc. Chem. Res.* **14**, 284–290 (1981).
3. J. Tao, A. D. Frankel, Electrostatic interactions modulate the RNA-binding and transactivation specificities of the human immunodeficiency virus and simian immunodeficiency virus Tat proteins. *Proc. Natl. Acad. Sci. U.S.A.* **90**, 1571–1575 (1993).
4. B. Honig, A. Nicholls, Classical electrostatics in biology and chemistry. *Science* **268**, 1144–1149 (1995).
5. F. Fogolari, A. Brigo, H. Molinari, The Poisson-Boltzmann equation for biomolecular electrostatics: A tool for structural biology. *J. Mol. Recognit.* **15**, 377–392 (2002).
6. H. Nakamura, Roles of electrostatic interaction in proteins. *Q. Rev. Biophys.* **29**, 1–90 (1996).
7. F. B. Sheinerman, R. Norel, B. Honig, Electrostatic aspects of protein-protein interactions. *Curr. Opin. Struct. Biol.* **10**, 153–159 (2000).
8. Y. Okuno, A. Szabo, G. M. Clore, Quantitative interpretation of solvent paramagnetic relaxation for probing protein-cosolute interactions. *J. Am. Chem. Soc.* **142**, 8281–8290 (2020).
9. B. Yu, C. C. Pletka, B. M. Pettitt, J. Iwahara, De novo determination of near-surface electrostatic potentials by NMR. *Proc. Natl. Acad. Sci. U.S.A.* **118**, e2104020118 (2021).
10. B. Yu, C. C. Pletka, J. Iwahara, Protein electrostatics investigated through paramagnetic NMR for nonpolar groups. *J. Phys. Chem. B* **126**, 2196–2202 (2022).
11. B. Tsang, I. Pritišanac, S. W. Scherer, A. M. Moses, J. D. Forman-Kay, Phase separation as a missing mechanism for interpretation of disease mutations. *Cell* **183**, 1742–1756 (2020).
12. A. K. Dunker, C. J. Brown, Z. Obradovic, Identification and functions of usefully disordered proteins. *Adv. Protein Chem.* **62**, 25–49 (2002).
13. V. N. Uversky, C. J. Oldfield, A. K. Dunker, Intrinsically disordered proteins in human diseases: Introducing the D^2 concept. *Annu. Rev. Biophys.* **37**, 215–246 (2008).
14. P. E. Wright, H. J. Dyson, Intrinsically disordered proteins in cellular signalling and regulation. *Nat. Rev. Mol. Cell Biol.* **16**, 18–29 (2015).
15. A. A. Hyman, C. A. Weber, F. Jülicher, Liquid-liquid phase separation in biology. *Annu. Rev. Cell Dev. Biol.* **30**, 39–58 (2014).
16. A. S. Lyon, W. B. Peeples, M. K. Rosen, A framework for understanding the functions of biomolecular condensates across scales. *Nat. Rev. Mol. Cell Biol.* **22**, 215–235 (2021).
17. R. K. Das, R. V. Pappu, Conformations of intrinsically disordered proteins are influenced by linear sequence distributions of oppositely charged residues. *Proc. Natl. Acad. Sci. U.S.A.* **110**, 13392–13397 (2013).
18. M. Sickmeier et al., DisProt: The database of disordered proteins. *Nucleic Acids Res.* **35**, D786–D793 (2007).
19. S. Müller-Späth et al., From the Cover: Charge interactions can dominate the dimensions of intrinsically disordered proteins. *Proc. Natl. Acad. Sci. U.S.A.* **107**, 14609–14614 (2010).
20. C. W. Pak et al., Sequence determinants of intracellular phase separation by complex coacervation of a disordered protein. *Mol. Cell* **63**, 72–85 (2016).
21. P. A. Chong, R. M. Vernon, J. D. Forman-Kay, RGG/RG motif regions in RNA binding and phase separation. *J. Mol. Biol.* **430**, 4650–4665 (2018).
22. B. Dutagaci et al., Charge-driven condensation of RNA and proteins suggests broad role of phase separation in cytoplasmic environments. *eLife* **10**, e64004 (2021).
23. T. H. Kim et al., Phospho-dependent phase separation of FMRP and CAPRIN1 recapitulates regulation of translation and deadenylation. *Science* **365**, 825–829 (2019).
24. K. Nakayama et al., RNG105/caprin1, an RNA granule protein for dendritic mRNA localization, is essential for long-term memory formation. *eLife* **6**, e29677 (2017).
25. Y. H. Jiang et al., Detection of clinically relevant genetic variants in autism spectrum disorder by whole-genome sequencing. *Am. J. Hum. Genet.* **93**, 249–263 (2013).
26. L. E. Wong, T. H. Kim, D. R. Muhandiram, J. D. Forman-Kay, L. E. Kay, NMR experiments for studies of dilute and condensed protein phases: Application to the phase-separating protein CAPRIN1. *J. Am. Chem. Soc.* **142**, 2471–2489 (2020).
27. T. H. Kim et al., Interaction hot spots for phase separation revealed by NMR studies of a CAPRIN1 condensed phase. *Proc. Natl. Acad. Sci. U.S.A.* **118**, e2104897118 (2021).
28. A. Patel et al., ATP as a biological hydrotrope. *Science* **356**, 753–756 (2017).
29. A. N. Milin, A. A. Deniz, Reentrant phase transitions and non-equilibrium dynamics in membraneless organelles. *Biochemistry* **57**, 2470–2477 (2018).
30. I. Alshareedah et al., Interplay between short-range attraction and long-range repulsion controls reentrant liquid condensation of ribonucleoprotein-RNA complexes. *J. Am. Chem. Soc.* **141**, 14593–14602 (2019).
31. K. Pervushin, R. Riek, G. Wider, K. Wüthrich, Attenuated T_2 relaxation by mutual cancellation of dipole-dipole coupling and chemical shift anisotropy indicates an avenue to NMR structures of very large biological macromolecules in solution. *Proc. Natl. Acad. Sci. U.S.A.* **94**, 12366–12371 (1997).
32. R. B. Stockbridge, R. Wolfenden, Enhancement of the rate of pyrophosphate hydrolysis by nonenzymatic catalysts and by inorganic pyrophosphatase. *J. Biol. Chem.* **286**, 18538–18546 (2011).
33. R. A. Alberty, R. M. Smith, R. M. Bock, The apparent ionization constants of the adenosinephosphates and related compounds. *J. Biol. Chem.* **193**, 425–434 (1951).
34. E. W. Martin et al., Valence and patterning of aromatic residues determine the phase behavior of prion-like domains. *Science* **367**, 694–699 (2020).
35. T. J. Nott et al., Phase transition of a disordered nuage protein generates environmentally responsive membraneless organelles. *Mol. Cell* **57**, 936–947 (2015).
36. J. Wang et al., A molecular grammar governing the driving forces for phase separation of prion-like RNA binding proteins. *Cell* **174**, 688–699.e16 (2018).
37. S. F. Banani, H. O. Lee, A. A. Hyman, M. K. Rosen, Biomolecular condensates: Organizers of cellular biochemistry. *Nat. Rev. Mol. Cell Biol.* **18**, 285–298 (2017).
38. S. Maharana et al., RNA buffers the phase separation behavior of prion-like RNA binding proteins. *Science* **360**, 918–921 (2018).
39. Z. Monahan et al., Phosphorylation of the FUS low-complexity domain disrupts phase separation, aggregation, and toxicity. *EMBO J.* **36**, 2951–2967 (2017).
40. B. Tsang et al., Phosphoregulated FMRP phase separation models activity-dependent translation through bidirectional control of mRNA granule formation. *Proc. Natl. Acad. Sci. U.S.A.* **116**, 4218–4227 (2019).
41. F. Delaglio et al., NMRPipe: A multidimensional spectral processing system based on UNIX pipes. *J. Biomol. NMR* **6**, 277–293 (1995).
42. J. J. Helmus, C. P. Jaroniec, Nmrglue: An open source Python package for the analysis of multidimensional NMR data. *J. Biomol. NMR* **55**, 355–367 (2013).
43. H. Geen, R. Freeman, Band-selective radiofrequency pulses. *J. Magn. Reson.* **93**, 93–141 (1991).
44. F. Wang, S. K. Ramakrishna, P. Sun, R. Fu, Triple-pulse excitation: An efficient way for suppressing background signals and eliminating radio-frequency acoustic ringing in direct polarization NMR experiments. *J. Magn. Reson.* **332**, 107067 (2021).
45. S. J. Gibbs, C. S. Johnson, A PFG NMR experiment for accurate diffusion and flow studies in the presence of eddy currents. *J. Magn. Reson.* **93**, 395–402 (1991).
46. D. H. Wu, A. D. Chen, C. S. Johnson, An improved diffusion-ordered spectroscopy experiment incorporating bipolar-gradient pulses. *J. Magn. Reson. A* **115**, 260–264 (1995).
47. A. Abragam, *Principles of Nuclear Magnetism* (Clarendon Press, Oxford, UK, 1961).
48. G. A. A. Saracino et al., Solvent polarity and pH effects on the magnetic properties of ionizable nitroxide radicals: A combined computational and experimental study of 2,2,5,5-tetramethyl-3-carboxypyrrolidine and 2,2,6,6-tetramethyl-4-carboxypiperidine nitroxides. *J. Phys. Chem. A* **106**, 10700–10706 (2002).